COMMUNICATION

Check for updates

Rolling contact bistable passive and active metamaterials

Mohammad Naghavi Zadeh, [iD] *[a] Fabrizio Scarpa [iD] [b] and Jonathan Rossiter [iD] *[a]

Negative stiffness and bistability are desirable properties to improve the speed and power of actuators, dissipate energy in shock absorbers, and provide stable switching mechanisms. However, most negative stiffness mechanisms cannot deliver large strain capacity, high force density and long fatigue life simultaneously due to plastic strain accumulation. We propose a new class of metamaterial featuring rolling flexible beam deformation that enables control over strain responses in architected materials. In addition, multiple rolling beams can be incorporated in a unit cell to significantly amplify the force density and metamaterials with rolling beams can be used as passive flexible structures or bistable actuators. The elastic properties of these metamaterials are examined through tensile tests and finite element analysis. Negligible changes in the force–displacement response are observed after more than 10 000 cycles. The performance of electroactive rolling versions are evaluated using dielectrophoretic liquid zipping actuation, demonstrating power amplification through snapping. Moreover, the rolling mechanism enables this bistable design to facilitate both linear and rotational motions, or a combination of both. This is demonstrated in applications including an efficient perching mechanism for drones and rapid-response grippers, illustrating the wide potential impact of this rolling contact metamaterial mechanism.

New concepts

We introduce rolling bistable passive and active elastic strips in mechanical metamaterials to overcome limitations of conventional negative stiffness mechanisms which cannot simultaneously deliver large strain capacity, high force density and long fatigue life due to plastic strain accumulation. Through a heuristic rational design, we present rotating walls that form a bistable unit cell through rolling contact. Using experimental tests and numerical simulations, we characterize both passive (externally driven) and active (through electrostatic zipping actuation) rolling contact metamaterials and study the effect of different geometrical parameters on its performance. Displacement controlled cyclic tests show long cyclic life with negligible changes in peak forces. In addition to large strain and long cyclic life, the number of rolling strips can be increased for greater force density. The highly tuneable features of the presented bistable passive and active rolling contact mechanism facilitate wide application from active metamaterials to low energy manipulators.

1 Introduction

Mechanical metamaterials have emerged as transformative tools in materials science and robotics by enabling the control of mechanical properties through the design of micro-architectures and unit cells. In soft robotics, flexible metamaterials allow for simplification of control through rationally designed continuous deformations and mechanical properties such as negative Poisson's ratio and negative stiffness.[1,2] Among several advanced properties achieved by metamaterials, negative stiffness and bistability offer a foundation for the realization of adaptive, energy efficient and responsive systems that enable functionalities such as energy dissipation and shock absorption,[3–6] programmable nonlinear mechanical response,[7,8] shape morphing,[9–11] and mechanical energy storage[12] or shape adaptation for specific functionalities, such as tuning of the electromagnetic response.[13] These attributes are increasingly being applied to robotic systems, where rapid, controlled transitions enabled by snapping are leveraged for locomotion, gripping, and actuation tasks[14,15] that are also observed in natural systems such as the Venus flytrap and Mantis shrimp.[16,17]

Within the domain of robotic systems – including actuators and active metamaterials – negative stiffness and bistability contribute significantly to the amplification of force and power,[18,19] with snapping helping to reduce the transition time between two states, leading to increased speed and efficiency.[20–22] At the same time, bistability alleviates the need for energy consumption to maintain the system in a stable

[a] School of Engineering Mathematics and Technology (SEMT), University of Bristol, Bristol BS8 1TW, UK. E-mail: jonathan.rossiter@bristol.ac.uk
[b] Bristol Composites Institute, School of Civil, Aerospace and Design Engineering (CADE), University of Bristol, Bristol BS8 1TR, UK

configuration against disturbances.[23,24] Multiple stable modes are also desirable for switch and memory storage applications, such as MEMS and binary micro-actuators,[25–30] self-holding valves,[31,32] and shape memory.[33]

Existing bistable and negative stiffness mechanisms mostly fall within limited geometrical categories: curved or buckled beams and shells such as dome-shaped shells and sinusoidal-shaped beams, in which the application of a mechanical load or other types of stimuli (such as magnetic field, electric field, temperature change, or pressure) contributes to switching the direction of curvature[34–39]; compliant mechanisms where flexible hinges provide localized deformation[7,40,41]; and origami and kirigami that enable large area and volume changes.[9,14,42–44] Also, bistable mechanisms exist for which two hinged non-collinear elements are constrained with an elastic spring.[45,46] Three important measures emerging from the design of any bistable mechanism are the maximum force through the displacement range (force capacity), the maximum strain (strain capacity), and the number of cycles before failure due to fatigue (life cycle). All bistable mechanisms in these geometrical categories are designed on the basis of a trade-off between force capacity, strain capacity, and life cycle.

Long life cycle is an important factor in the design of meta-materials, especially if the replacement process is non-trivial, such as meta-biomaterials and meta-implants for biomedical applications.[47–51] In these cases, the fatigue life is associated with peak stresses and strains within the microstructure, which limit the maximum force and strain at the macro scale. In existing negative stiffness designs, such as prestressed (buckled) or curved beams and shells, high cycle lifetimes are achieved by limiting deformation to low strains at both micro and macro scales.[10,52,53] However, fatigue performance degrades considerably if higher forces and strains are required, and multidisciplinary studies are required to optimize fatigue life in these conditions.[54,55] Compliant hinged metamaterials can improve the life cycle, but force capacity will be small and achieving long life cycles is still challenging due to stress concentrations at the hinges.[41] Further, if hinges are modified with flexible materials to mitigate stress concentration, key features of negative stiffness and bistability may disappear.[56] Combining high strain capacity, high force capacity, and high fatigue life at the same time remains an unresolved challenge.

To address this challenge, it is important to alter the existing deformation mechanism in metamaterial micro-architectures for a mechanism that achieves large deformations within a controllable, and useful, range of peak stresses. Current meta-material micro-architectures are mainly made from bar elements that sustain axial load or beam elements that sustain bending moments. Truss lattices, like face-centered cubic tessellations and 2D beam assemblies such as honeycombs (Fig. 1a) are prime examples of the use of bar and beam elements, respectively. In addition, these deformation mechanisms can be exploited in larger deformation mechanisms in other embodiments. For example, compliant hinges of rotating cube tessellations and origami structures can be modeled as thin beams of short span, where bending (primary) leads to rotational (secondary) deformation (Fig. 1a). These bar and beam elements are strongly prone to fatigue failure at stress concentration points and joining interfaces. Moreover, the force capacity and the strain capacity in these structural elements act in opposite ways, that is, a large strain capacity is achieved at the cost of reducing the force capacity, and *vice versa*.

We propose here a metamaterial mechanism that addresses the challenges highlighted above and achieves capabilities that have not been simultaneously demonstrated: large strain capacity, large and tuneable force capacity and long life cycle. To overcome the undesirable interplay between force and strain, a rolling contact of flexible strips is introduced (Fig. 1b), in which large bending of the strips is the primary deformation mechanism. While peak stresses are controlled by tuning the radius of curvature, the rolling amplifies the strain capacity, independently of stress. Previously, rolling contact has been used to create Rolamite as a linear constant-force sensor[57] and for developing rolling joint mechanisms,[58–60] also used in chiral rotating metamaterials.[61] However, the combination of linear and rotational motion with bistability has not been previously achieved. Here, the proposed metamaterial consists of two flexible strips positioned back to back and constrained together at one end, while the other end is bent and attached to a wall that provides the contact surface for rolling. To maintain these prestressed strips and walls in place, a constraint connects the walls, while allowing their rotation within predefined limits (see SI-1 for further details). This prestressed configuration (Fig. 1c) is in a stable state that features strips rolling into the channel created by the walls through the application of a compressive load in the rolling direction. During the rolling process, the walls initially form a converging channel, hence the bending curvature of the strips increases (*i.e.*, stress and strain energy increase). After passing through the minimum channel width section, the walls begin to rotate and form a diverging channel, which reduces the strain energy along the rolling direction. This generates a negative stiffness effect, until reaching the second stable position.

In this research, we introduce details of the proposed mechanical metamaterial and investigate the role of different geometrical parameters on its performance. We explore the actuation capability of the metamaterial using electrostatic forces as a potential architecture for an artificial muscle. We also show the versatility of this metamaterial design in achieving bistable linear motion, rotational motion, or combination of both as demonstrated in a perching mechanism and a rapid snapping gripper. We also demonstrate multi-strip design as an important strategy to maintain peak stress levels low while achieve higher force capacity, while existing bistable mechanisms such as curved shells, curved beams, and compliant hinge mechanisms suffer from high stress points (Fig. 1f).

1.1 Design of rolling contact metamaterial

The geometrical parameters required to define the unit cell of the rolling contact metamaterial are presented in Fig. 1d. Each unit cell has an initial stable length L and width W made by two
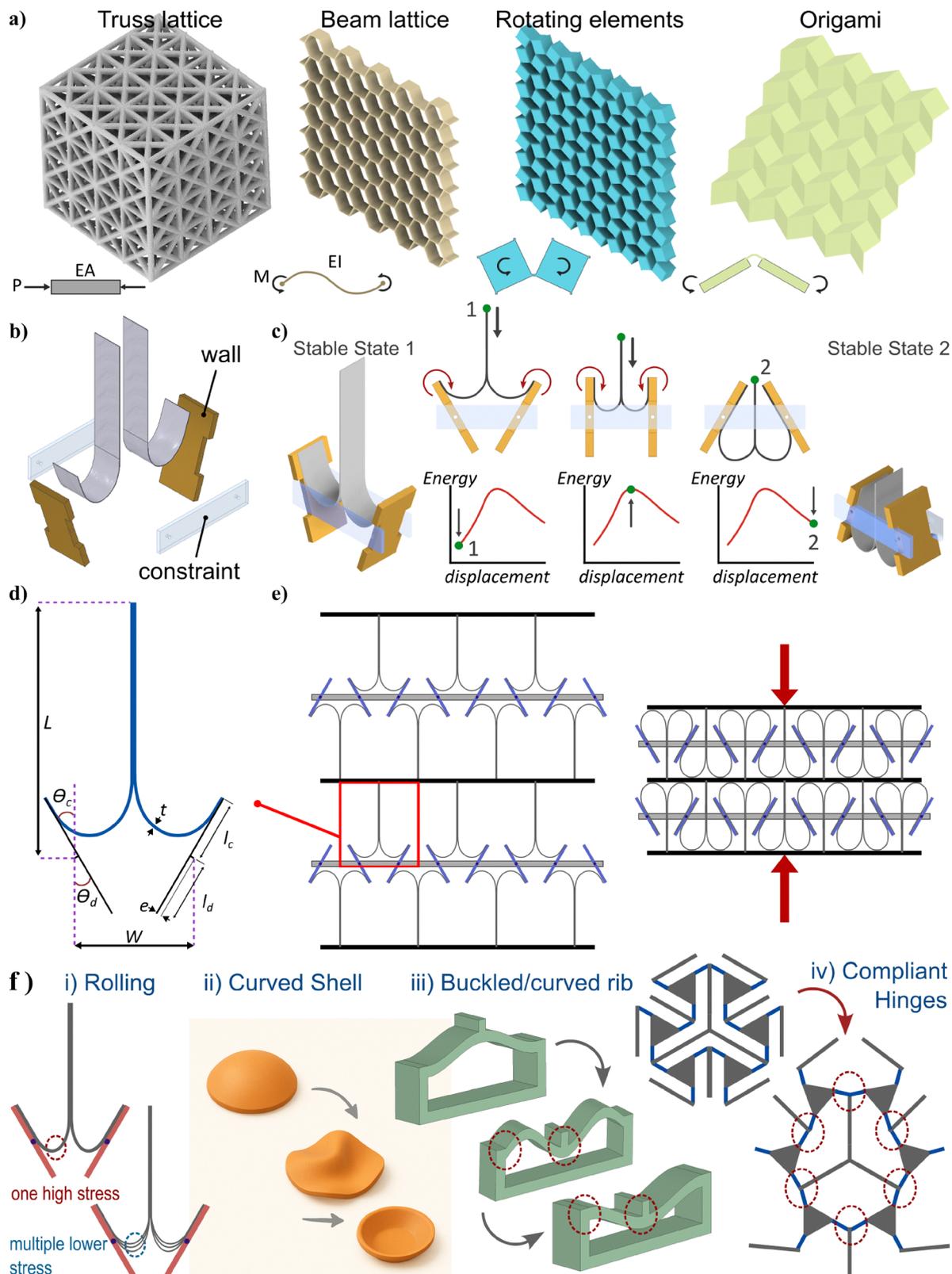
Fig. 1 Metamaterial design. (a) Frequently used primary and secondary deformation mechanisms in different classes of metamaterials, (b) main components of the bistable rolling metamaterial with (c) initial and compressed configurations and energy states 1 and 2. (d) The parameter definitions in a unit cell and (e) its representation in a compressible lattice. (f) Geometrical comparison of the (i) rolling bistable metamaterial with (ii) curved shell, (iii) curved beam, and (iv) compliant hinged bistable metamaterials.

strips of length l and thickness t. For a single isolated unit cell, the wall lengths in the convergent (l_c) and divergent (l_d) sections could be different, however in the tessellation of Fig. 1e ($l_c = l_d$) the angles of the walls can be independent inside the convergent (θ_c) and divergent (θ_d) sections ($\theta_c \neq \theta_d$, see SI-1). Each wall has a thickness T and the center of rotation is considered at the center-line of the wall; therefore, the contact surface has an eccentricity $e = T/2$, which implies that the practical minimum width of the channel at the contact surfaces is $W - 2e$. To understand the role of different geometrical parameters, experimental quasi-static tensile tests and numerical simulations are performed. The characterization study covers independent parameters including width W, angle θ and eccentricity of the wall e. The thickness of the wall T and eccentricity e are dependent, hence T is not characterized separately. In addition, an approximate statistical-analytical model is developed and presented in Supplementary Information (SI-1) that studies the relationship between length of strip and other parameters, which can also be used for parameter optimization.

2 Results and discussion

2.1 Mechanical characterization

Mechanical tests are performed on a rig (SI-2) that allows the evaluation of configurations with varying width W and angle θ, when equal angles on convergent and divergent sides are considered. Three sets of stainless steel strips with thicknesses of 100, 150 and 200 micron (see Section 4 for details) were tested using the rig, for widths ranging from 40 to 90 mm at every 10 mm step, and angles from $\theta = 5°$ to $\theta = 45°$ with $5°$ steps. The free end of the strips was connected to a load cell at $L = 23$ mm and measuring the axial force F_x (Fig. 2a). The results are visualized according to width and angle, as shown in Fig. 2b where the maximum force for each value of W and θ is highlighted. The range of displacement in tests was 180 mm, which is equal to 78% strain for the given dimensions. The two factors affecting the transition of the strips through the minimum width section are buckling and yield stress. In these experiments, as the length of the strips were long compared to thickness, buckling was the main failure mechanism that precluded transition through the minimum width section and reaching the second stable point (highlighted in grey).

Force–displacement diagrams are presented in Fig. 2c–e for $W = 70$, 80, and 90 mm at $t = 200$ micron, respectively. Force–displacement curves at constant width but different angles overlap each other on their negative stiffness interval and pass through the zero-force point at the same displacement. In addition to experimental tests, finite element analysis is used for further characterization where half of the model with symmetry conditions (a rigid wall with no friction replicating back-to-back contact between two strips) and considering geometrical nonlinearities is studied using two explicit dynamic steps with details presented in SI-3. The results of these numerical simulations are verified with experiments, as shown

in Fig. 2c(i) for three angles at $\theta = 5$, 10, and 15 degrees. The trends of strain energy, maximum stress value in the strip (S_{max}), and the reaction force in the transverse direction (F_y) are evaluated using simulations. The position and maximum value of the strain energy (Fig. 2c(ii)) are the same, while the position and value of S_{max} and F_y change with the angle (Fig. 2c(iii)). While axial forces F_x become negative as the strips roll past the pivot point (the point of minimum channel width), transverse forces F_y are always positive and have larger values than F_x (Fig. 2c(iv)). Fig. 2f highlights the effect of the channel width over the axial forces, for constant thickness and angle. Smaller channel widths lead to higher curvatures and larger stresses; therefore, higher minimum and maximum axial forces (F_x) and stiffness (both positive and negative) are expected when the width reduces. The absolute values of maximum and minimum forces $F_{x_{max}}$ and $F_{x_{min}}$ increase when the angle increases and when the width becomes smaller (Fig. 2g).

The change of $F_{x_{max}}$ is significantly larger than the variation of $F_{x_{min}}$ when the angle increases, and the absolute value of $F_{x_{max}}$ increases approximately linearly with increments of the angle (Fig. 2h). In addition, the displacements at which $F_{x_{max}}$ and $F_{x_{min}}$ are respectively maximum, change considerably with the angle (Fig. 2i). One critical feature of the performance of bistable metamaterials in robotic applications is the work done on the system to achieve the target displacement (strain). Fig. 2j depicts the effect of the width and angle on the work done. The net work done on the metamaterial is negative when both angle and width are small. This means that the metamaterial will deliver net positive work, although it requires an activation energy to pass through the energy barrier. The effect of the eccentricity (e) is also investigated using numerical simulations. As thickness of the rotating wall reduces the effective width of the channel, therefore, the effect of increasing the eccentricity e is expected to be similar to the reduction in channel width W in terms of force and strain energy as shown in Fig. 2k and l, respectively, for three different values of eccentricity $e = 0.0$, 0.03, and 0.1. In Fig. 2k, a Gaussian data smoothing is applied on five data point intervals. In addition to the geometrical parameters, the constitutive material of the strips also significantly affects the mechanical performance. The maximum force (F_{max}) ratio of an arbitrary material with respect to steel is equal to the bending rigidity (EI) ratio of the strips, as confirmed by further experiments in SI-1.8.

While force–displacement results in a tension-compression cycle overlap for a single unit cell, the behavior could be different in a lattice. Therefore, a lattice demonstrator with three rows of seven cells is assembled using 150 micron thick stainless steel strips where $W = 45$ mm, $L = 70$ mm, and $\theta = 30$ degrees. The initial length (l_i) of each row in compressed configuration is 50 mm (Fig. 3a). When stretched into the second stable position, the final length (l_f) of each row is 160 mm, resulting in a total strain capacity of $\varepsilon = 2.13$ ($\varepsilon_r = 0.71$ per row). The force–displacement diagram of the lattice (Fig. 3a) is shown for one tension-compression cycle (see SI-5). The force–displacement curves of the lattice do not overlap in this case, resulting in hysteresis, with hysteresis area in
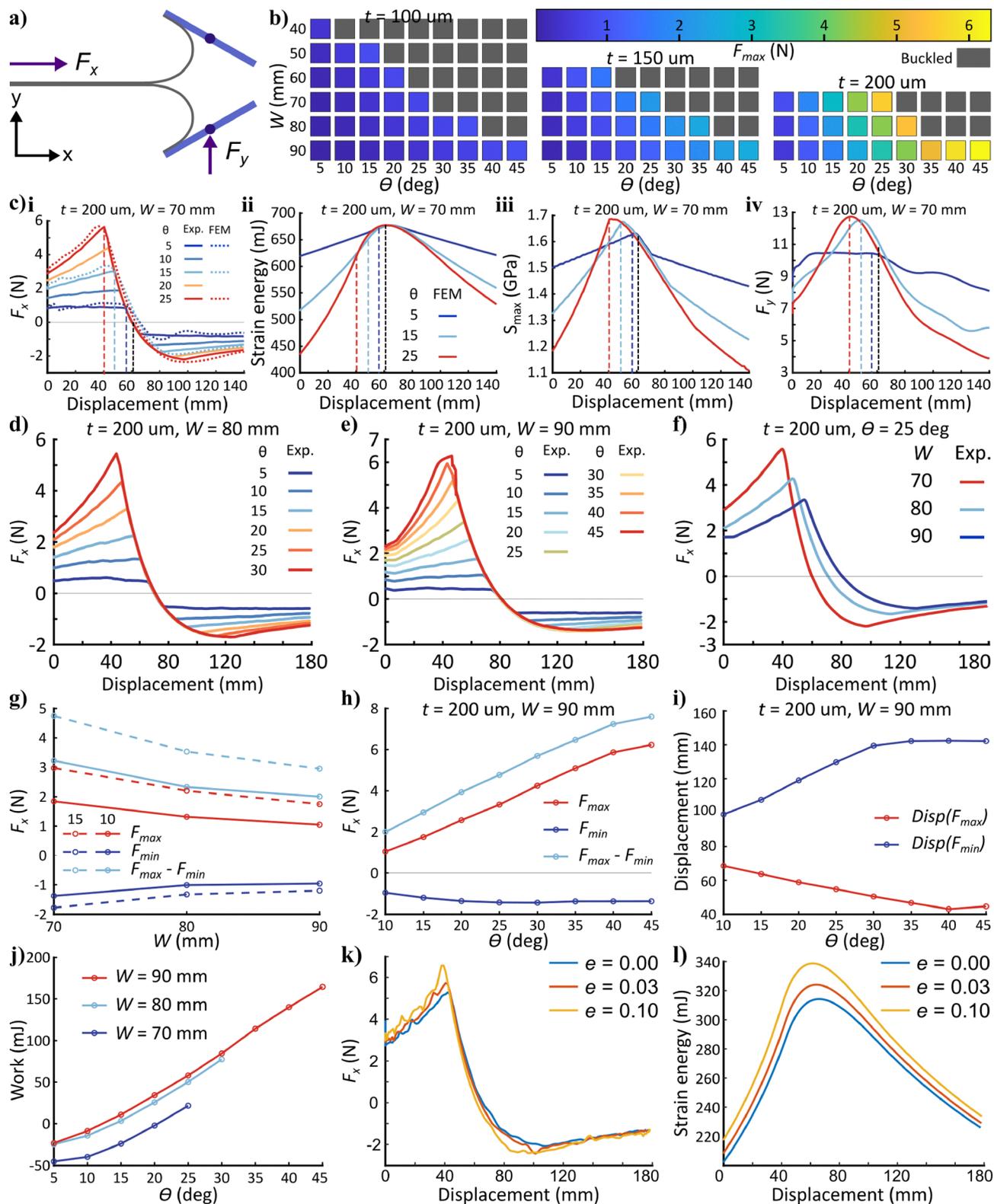
Fig. 2 Mechanical characterization. (a) Definition of forces and coordinates system in the unit cell. (b) Peak axial force as strips transition through channel for different widths W, angles $\theta = \theta_c = \theta_d$ and thicknesses $t = 100, 150, 200$ micron. Successful transitions shown in color and buckled failures shown in grey. (c) Experimental data and numerical simulations (Abaqus 2023) to characterize the (i) axial force F_x, and FE analysis results to characterize (ii) strain energy, (iii) maximum stress in strips and (iv) the transverse force F_y for $t = 200$ micron and $W = 70$ mm case. (d)–(f) show the evolution of axial force with displacement for different angles θ: (d) $W = 80$ mm and (e) $W = 90$ mm and for different widths (f) $\theta = 25°$. (g) and (h) show trends of axial peak force F_x vs. width W and angle θ respectively. (i) shows displacements corresponding to force peaks and (j) shows work done on the bistable mechanism at different angles θ. (k) Effect of wall eccentricity e on force–displacement, and (l) strain energy profile.
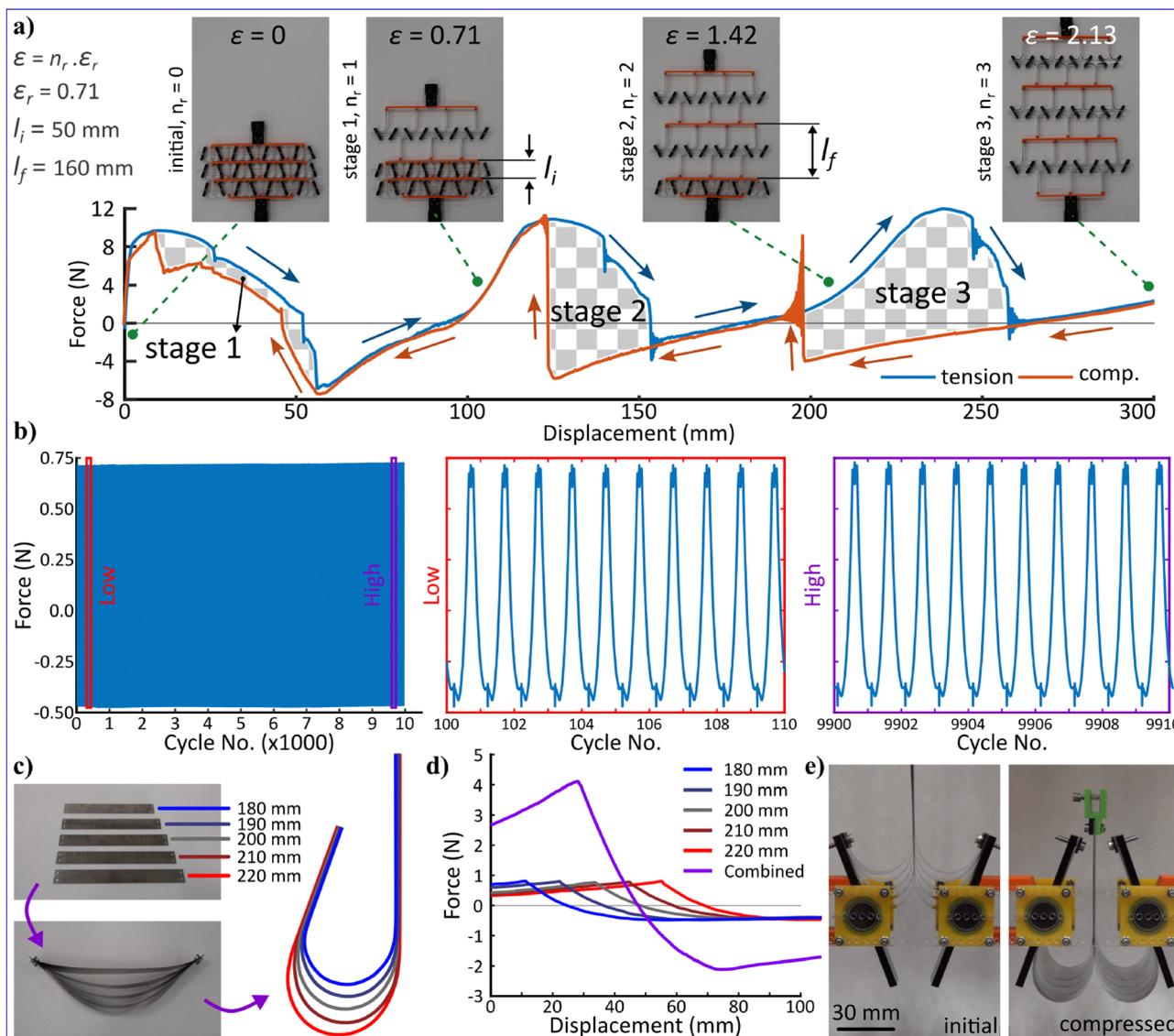
Fig. 3 Mechanical performance analysis of a metamaterial lattice. (a) Lattice load cycle analysis in tension and compression. (b) Fatigue and cyclic life evaluation in 10 000 displacement-controlled cycles. (c) Strip multiplication by tailoring strip length and bonding together. (d) Force–displacement diagrams comparing single strips of a range of lengths with the combined five strip set. (e) Initial and compressed configurations of the five strip set.

stage 3 > stage 2 > stage 1. The negative forces at each stage indicate that the lattice passes an energy barrier and moves to a new stable mode. These results show that the metamaterial has an effective bistable behavior by using rolling contact with a large strain capacity ($\varepsilon \geq 2$). In terms of deformation sequence, additional degrees of freedom, including rotation, emerge in a lattice (see SV-3) due to asynchronous snapping of unit cells in a row caused by imperfections in assembly and manufacturing. To control the sequence and mode of deformations in lattice metamaterials, two approaches exist: passive and active. Passive approaches can utilize the rational use of imperfections within a tessellation to achieve a desired deformation sequence and shape.[62] In active approach, a transduction method will be employed to tune the deformed shape of the lattice globally or locally.[63] While active approach is more complex to implement, it provides the flexibility to perform adaptive spatial control within the lattice to achieve a multitude of shapes and deformation sequences.

It is next important to ascertain whether it is possible to combine low fatigue (high cyclic life) and high force density features with high strain capacity, which has been the limit of bistable metamaterials and mechanisms so far. As the strips are the only components undergoing bending deformation in rolling strip structures, the fatigue behavior of the metamaterial is inherited from the fatigue behavior of the strips. To investigate the fatigue life, displacement controlled cyclic loading for 10 000 cycles is performed on a unit cell with 100 micron stainless steel strips ($W = 60$ mm, $\theta = 25$ deg.) with the displacement range covering the maximum and minimum forces (*i.e.* showing full transition between two stable states).

Fig. 3b shows that the difference in the maximum and minimum load at both small and large number of cycles is negligible, confirming the effectiveness of using low fatigue metallic strips to achieve high life cycle for the metamaterial.

Prior studies consistently show that bistable/negative-stiffness systems can remain operational over thousands of cycles while exhibiting notable cyclic degradation in force- or energy-related performance metrics. Shang *et al.* reported bistable auxetic mechanisms in acetal resin that preserved bistability up to 10 000 cycles without catastrophic failure, yet the attainable load amplitude deteriorated substantially, reaching 40% reduction after 1085 cycles in some geometries.[41] Similarly, cyclic tests on 3D-printed PLA negative-stiffness metamaterials showed a marked decline in per-cycle energy absorption, with reductions of 25–50% after 30 cycles depending on unit-cell geometry.[64] For thin CFRP tapes (0.25 mm thickness), peak stress also decreased measurably under repeated loading: an initial peak stress of 4 MPa was followed by more than 10% reduction after 10 000 cycles.[53] Comparable fatigue-induced efficiency losses have been observed even at nanoscale actuation using biomolecular systems, where actuation efficiency drops by 20% by 10 000 cycles.[65] Collectively, these results provide fatigue comparisons based not only on "survival" or bistability retention, but also on cycle-dependent decay of peak force/stress and energy/actuation efficiency, which can be substantial and strongly design-dependent. In this case, the advantage of rolling strip mechanisms in low fatigue and long life-cycle is evident, where negligible change in peak forces after 10 000 loading cycles were observed (Fig. 3b).

The force density of the unit cell is defined as the maximum force (F_{max}) per volume ($V = W \cdot L \cdot b$, where b is out-of-plane width). An important advantage of the rolling mechanism is the possibility of adding rollers in parallel, which allows for amplification of the force within the same volume. To achieve parallel rolling, the strips should have a length difference. Fig. 3c shows five metal strips ($t = 100$ micron) with 10 mm variation in length ranging from 180 to 220 mm. The ends of five strips are aligned and clamped together, resulting in prestress and forming a bow shape. When the ends are constrained in a unit cell, a multi-strip roller is formed. Force–displacement diagrams of individual unit cells for strips of different lengths are presented in Fig. 3d where L is constant for all five cases ($W = 60$ mm, $\theta = 25$ deg.). As geometrical parameters and thickness of strips are the same, the force–displacement diagrams are similar but with a shift in displacement equal to the difference in length, which is 10 mm. When five strips are combined (Fig. 3e), the maximum and minimum force values are approximately five times those of single strips. As the length difference between strips are equal and the number of strips is odd, the displacement at which force becomes zero in the combined set is equal to that of the individual strip with $l = 200$ mm. While a set of five strips with different lengths is investigated here, it is possible to reduce the length increment and increase the number of combined strips to achieve much higher force density.

While stress and strain are dependent in most mechanical metamaterials and engineering structures, this rolling mechanism and geometrical features allowed the independency of stress from strain. A statistical-analytical approach is presented in SI that allows calculation of the strain (SI-1.5) and stress (SI-1.6). The methodology shows that peak stress depends on the elastic modulus of the strip's material E, thickness of the strip t, and maximum curvature of the strip, which depends on the width W and angle θ. In addition, maximum strain depends on the length of the strip l_{s}, length of the wall ($l_{c} + l_{d}$), and angle θ. Therefore, stress and strain can be tuned using geometry and material independently.

As a conclusion, these results confirm the attractive properties of the bistable rolling strip metamaterial including large strain capacity, long cyclic life and high force density. These characteristics can provide a significant improvement in the performance of different passive and active structures for diverse applications including robotics. To facilitate use in robotics we next propose and demonstrate electrostatically actuated bistable active metamaterials for future artificial muscle applications.

2.2 Actuation study

In addition to engineered mechanisms – including those presented above – natural striated muscles also present negative stiffness[66] and multistability.[67] The hierarchical structure of a natural muscle, from the macro scale skeletal muscle to the micro scale sarcomere, is presented in Fig. 4a. The proposed bistable metamaterial lattice mimics the sarcomere structure, where strips are analogous to myosin and rotating walls mimic the role of actin, against which the myosin moves (Fig. 4b). Focusing on the actuation mechanism, the rolling contact acts similar to zipping, where the gap between the strip and wall decreases to zero as the structure compresses and the zipping point progresses along the wall. Dielectrophoretic liquid zipping (DLZ)[68] is an electrostatic actuation mechanism that exploits zipping to generate mechanical forces and is a good candidate for the creation of an active bistable metamaterial using rolling contact. In addition, DLZ allows developing a proof of concept actuator in mesoscale for a potential MEMS actuator based on the proposed metamaterial. Moreover, a bistable architecture in previous electrostatic actuators based on DLZ and HASEL[31,68,69] in large scale was missing, hence, this bistable meta-actuator can fill the gap.

To achieve the electric field required for zipping actuation, a voltage is applied between the strip and the wall. Fig. 4c illustrates the modification required on the wall to achieve DLZ actuation. Metallic strips are conductive and act as one electrode, facilitating connection to electrical ground in this case. To provide a counter electrode on the wall, its surface is covered with a conductive tape, over which is applied an insulating layer to stop short circuits. To create the electric field, a high voltage (10 kV) is applied between the wall (positive electrode) and metal strips (ground electrode). A drop of dielectric liquid (in this case silicone oil) is applied at the zipping gap between the strip and the wall, amplifying the electric field and electrostatic forces significantly.
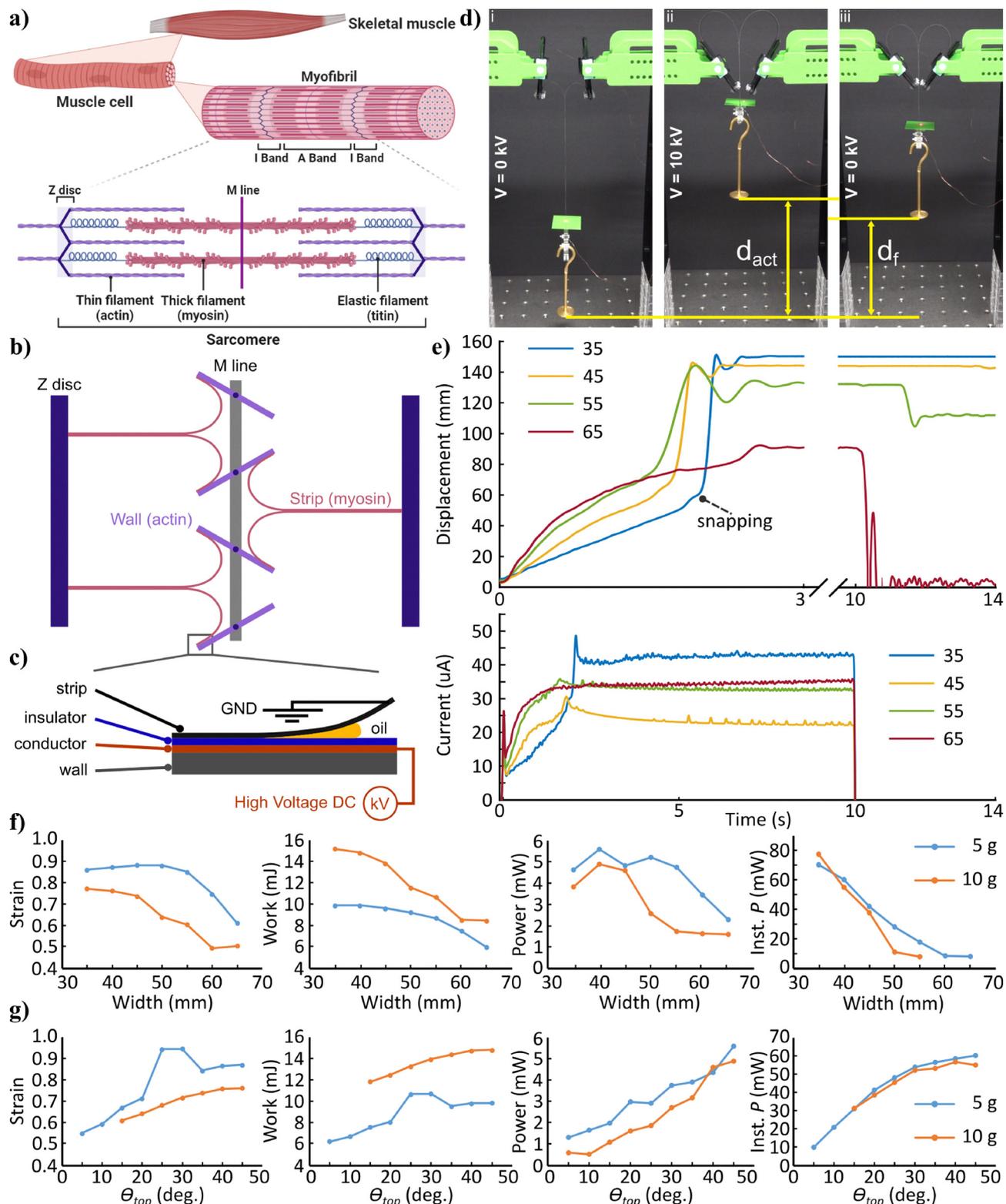
Fig. 4 Actuation mechanism and performance. (a) hierarchical structural of biological muscle. (b) Bioinspiration from the muscular sarcomere in active rolling contact bistable lattice metamaterial. (c) The modification of the walls for DLZ actuation. (d) Actuation demonstration of a bistable unit cell in (i) initial, (ii) actuated, and (iii) resting configurations. (e) Variation of displacement and current with time for different channel widths W. (f) The actuation performance data including strain, work, power and instantaneous power (snapping) for different widths (W) and (g) for different angles (θ_d).

The aim of actuation study is understanding the role of geometrical parameters on the actuation performance. Therefore, actuation study is performed on a unit cell, which represents the lattice. Using experimental isotonic tests (constant load), the effect of geometrical parameters on the actuation performance was studied where a range of widths from 35 to 65 mm (5 mm interval) was covered using 70 micron stainless steel strips ($\theta_c = 5°$). Actuation across a range of angles from $\theta_d = 5°$ to $\theta_d = 45°$ ($5°$ interval) were also studied. As the unit cell represents the lattice, the lengths of the wall in convergent and divergent sections were equal ($l_c = l_d$). The initial and actuated states of the unit cell are shown in Fig. 4d (see SI-6) where a 10 g mass is lifted. Depending on the geometrical parameters and the external load, five cases were observed: (1) the mass is lifted, the unit cell snaps, and the final displacement (d_f) after voltage cut-off remains the same as actuation displacement (d_{act}), (2) the mass is lifted and the unit cell snaps but $d_f < d_{act}$, (3) the mass is lifted and the unit cell snaps but the mass loading is heavy enough to drop to initial position after actuation is removed, (4) the mass is lifted but the work done by electrostatic forces is not enough to pass through energy barrier, hence no snapping, and (5) the mass is too heavy to lift.

Fig. 4e presents the displacement and current profile with respect to the time to lift a 5 g mass where a voltage of 10 kV was applied for 10 seconds. The smallest width ($W = 35$ mm) provides the highest stored elastic energy; therefore, the strain rate after snapping is also the highest and actuation and final displacement are equal. As width increases, the actuation displacement and strain rate after snapping reduce. The strips are like a spring and the energy barrier is like the latch (similar to cascading effect[70]); hence, the higher the stored strain energy in strips, the higher the speed and power after snapping. However, electrostatic forces must be large enough to push the compressed strips through the energy barrier. In terms of final displacement, the $W = 55$ mm case shows $d_f < d_{act}$ where the drop in final position occurs 1–2 seconds after the voltage was removed, which can be explained by the self-locking behavior of DLZ actuators.[71] For $W = 65$ mm, the snapping is not effective as stored energy becomes much smaller and the mass immediately drops after voltage cut-off. This class of actuator acts like a capacitor and the current due to the leakage of insulator is correlated with the area and displacement. This suggests that leakage current may be used for simultaneous sensing of actuator displacement.[72,73] This ability of actuation, self sensing, and use of bistability as a binary mechanical memory paves the way for the use of this active bistable metamaterial for intelligent matter applications.[74]

The performance of the DLZ actuation is evaluated for different widths (while $\theta_d = 45$ deg. for all cases) and different angles (while $W = 40$ mm for all cases) where strain, work, power and instantaneous power are evaluated. In case of bistable actuators, the sudden change in strain rate at the snapping point causes an increase in instantaneous power. All results are reported for two suspended masses of 5 g and 10 g. When increasing the widths (Fig. 4f), all four performance indicators in general show a declining trend, while the power trend shows a maximum at 40 mm widths before declining. When angle increases (Fig. 4g), all four actuation performance indicators increase. These results show that the best performances could be achieved for the smallest width W and largest angle θ_d. In these tests, the length of converging and diverging parts of the wall were equal ($l_c = l_d$). If l_c is minimized, the average power will further increase. The average power figures reported here (up to ≈ 6 mW) are much higher than previous DLZ-based actuators (less than 2 mW)[75,76] as a result of the large strain capacity of the mechanism and snapping that significantly increases speed of actuation. Using high voltage actuators on or in human body is a future possibility if suitable insulation is used and the peak electrical current is below safety limits for the human body.[69]

In this study, there was no voltage applied between the strips as a short circuit occurs due to lack of insulation. If an insulator such as PVC tape and a droplet of dielectric liquid are applied to the strips and a voltage is applied, zipping actuation is initiated which returns the mechanism to its first stable mode. The actuation mechanism will be similar to RoboHeart contraction mechanism previously studied.[76]

2.3 Utilizing linear and rotational motions simultaneously: bistable perching mechanism

Perching mechanisms are used by birds to save energy and to rest in a stable stationary state and a similar approach has been pursued for bio-inspired aerial robots.[77] Stable perching enables resistance against both linear loads and moments (Fig. 5a); however, replicating the effective perching mechanism of birds in aerial robots can lead to complex and heavy designs.[78] Bistable mechanisms have been introduced to reduce perching complexity by passive activation of gripping claws when they make contact with the target[79] and to increase the linear load capacity using locking mechanisms,[80] but mechanisms that focused on hanging from the target have not supported moment loading. Using spring-loaded claws[81,82] or curved-tape bistable perching mechanisms,[83] moments can be resisted but increasing the gripping (linear) force capacity requires higher stiffness and higher activation forces that demand activation by drone impact on the target and risking the survivability of drone. Using the proposed rolling contact bistable mechanism, these challenges can be overcome because the linear motion of the strips can be combined with rotational motion of the walls to achieve activation and grasping. Hence, the drone equipped with our rolling contact perching mechanism can hold stable on a target both vertically and at an incline (Fig. 5b).

Fig. 5c illustrates the details of the perching mechanism design in initial and final configurations. The mechanism includes a foot that connects to the drone at one end and connects to the rotating walls through hinges at the other end. A linear sliding slot controls the range of motion using a sliding stopper plate, which is is connected to the rolling strips. The distance between the wall hinges is the width (W) discussed previously, which imposes the limit for the maximum diameter (D) of the target that the mechanism can grasp. The perching
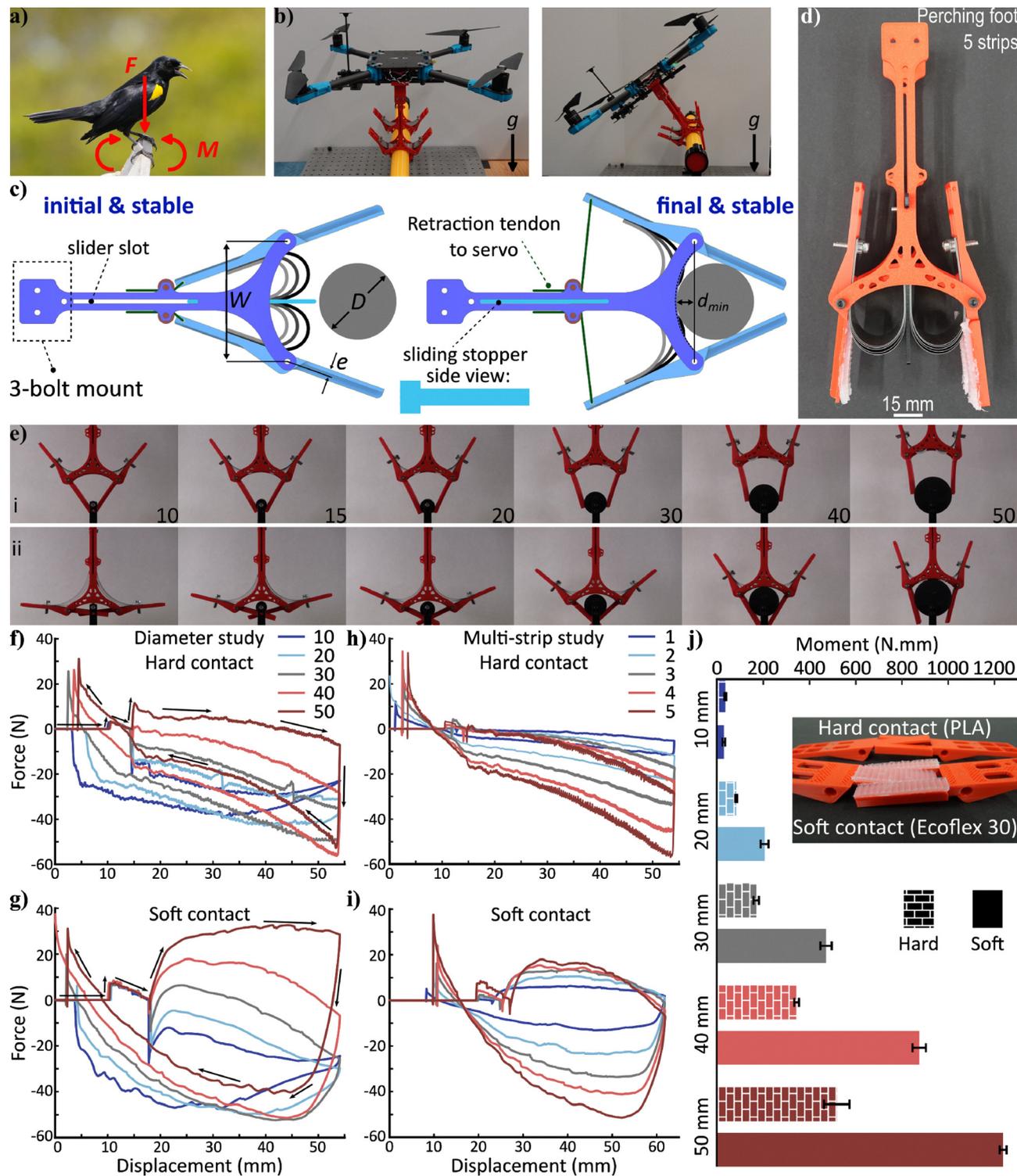
Fig. 5 Bistable rolling contact perching mechanism. (a) Bird perching resists both axial load and moment. (b) Perching mechanism based on bistable rolling mechanism supports both axial load and moment. (c) Design details of the bistable rolling perching mechanism. (d) An assembled model of the perching mechanism with a set of five metal strips. (e) The grasping configuration of the perching mechanism (i) immediately after snapping and (ii) at the rest position for different target diameters (D = 10, 15, 20, 30, 40, 50 mm). Force–displacement response of a full grasp/release cycle for different target diameters with (f) hard contact surface (PLA) and (g) soft contact surface (silicone). Responses for different number of strips between 1 and 5 are shown in (h) for hard contact and (i) for soft contact. The moment capacity of the perching mechanism for different target diameters and hard and soft surfaces (inset shows the contact surface with and without soft silicone pads).

mechanism is activated when the target contacts the sliding stopper plate and the strips and pushes them in past the snapping point. While the activation mechanism is passive and contact-based, resetting the mechanism requires an actuator such as a servo motor to pull retraction tendons connected to the walls. As initial and final configurations show, the walls act as rigid claws and once the target pushes the strips/stopper-plate into the negative stiffness zone, the mechanism rapidly snaps and grasps the target (see SI-7).

To characterize the performance of the perching mechanism, an example was assembled (Fig. 5d) using five 200 micron thick stainless steel strips where the foot (W = 60 mm) and the walls were 3D printed using PLA. The friction and flexibility of the contact surface can play a significant role in mechanical performance, therefore two types of surface were considered: hard contact (PLA) and soft contact (silicone pads – Ecoflex 30). The gripping force capacity was tested on a tensile test machine where targets with different diameters were installed. Fig. 5e illustrates the configuration of the perching mechanism immediately after snapping post-contact (i) and at the lowest rest position (ii). The force–displacement results for different target diameters are presented for both hard (Fig. 5f) and soft contact (Fig. 5g) cases. One important feature of this bistable rolling mechanism is the ability to set the activation displacement. The larger the activation displacement, the larger the activation force. In these tests, the activation displacement was approximately 4 mm and 7 mm for hard and soft contact, respectively, resulting in average activation forces of approximately 3 N and 7 N. In hard contact, for target diameters up to 40 mm, the grasping force at the beginning of contact (Fig. 5e(i)) is less than or equal to zero while stiffness is negative, which means that the perching mechanism will pull the drone down to the stable perching position (Fig. 5e(ii)). However, for the 50 mm target, the force post-contact is initially positive but stiffness is negative, which means that drone should exert a downward force (12 N) to reach the rest position. In the soft contact case, the target diameter where negative force and stiffness exist post-contact reduces to 20 mm while the stiffness remains negative up to 40 mm diameter, while for the 50 mm target, both stiffness and force are positive, which is not desirable. Therefore, hard contact is more desirable for grasping force in terms of range of target diameters.

Once the stable perch has been reached, we reverse the direction of displacement (*i.e.*, perching mechanism is moved upwards) and the force changes as the perching mechanism resists opening. In this condition, the highest grasping force capacity recorded is for a hard contact and a 40 mm target, showing 56.9 N resisting force. In the soft contact case, the shear deformation of silicone pads results in a change in the maximum grasping force displacement compared to the hard contact, and a maximum resisting force of 52.3 N for a 30 mm target is observed. Hence, the hard contact provides a better performance in terms of grasping force compared to the soft contact case, with a specific force (*i.e.*, mass normalized) of 514.9 N kg^{-1} being achieved. However, these figures can be further improved by making the feet of the architected material from stiffer and lighter materials, and also by increasing the

number of strips. The effect of different number of strips was also evaluated with samples with 1 to 5 strips (Fig. 5h and i for hard and soft contact, respectively). As expected, the absolute values of the forces and stiffness increased by increasing the number of strips, while the maximum grasping force increased about 11 N by adding each additional strip. One strip generated a specific force of 183.2 N kg^{-1}, which increased by increasing the number of strips. Therefore, the optimum configuration would have the largest number of strips and the lowest foot and walls mass.

In addition to the grasping force, a major benefit of the presented perching mechanism is the moment capacity to support the drone's angular position while resting on the target. Fig. 5j presents the moment capacity of hard and soft contact perching mechanisms for different target diameters. It is evident that the soft contact has a major advantage in terms of moment loading, with the moment capacity of the soft contact being 2.54 times larger than that of the hard contact for a 40 mm target. Therefore, the selection of a hard *versus* soft contact will depend on the mass and dimensions of the drone.

2.4 Utilizing rotational motion: rolling contact bistable gripper

One advantage of the bistable rolling contact mechanism is the potential to generate both rotational and linear motion. While the use of pure linear motion was demonstrated in passive/active lattice cases and the combination of linear and rotary motion was shown in perching mechanism, it is possible to utilize the rotational motion only for rapid bending applications such as fast bistable grippers. Many different types of grippers for different applications have been developed.[84] A bistable gripper with rapid actuation and long cyclic life is of great interest within the robotics community. To achieve a rotational motion, one wall of the mechanism should be fixed and the other wall free to move (Fig. 6a). The activation mechanism is a tendon connected to an actuator, such as servo motor, that applies a tensile force F_a directly on the walls and rotates them until they become parallel, after which snapping occurs. Similarly, the return mechanism is based on a retraction tendon returns the strips to the initial stable state. Each wall in a unit cell rotates by an angle $\theta = \theta_c + \theta_d$, while the rotational angle transferred from one cell to the next is $2(\theta + \varphi)$ where φ is the inclination angle of the contact surface. Considering the results in Section 2.1, the unit cell of a gripper mechanism is initially in its second bistable mode (open state), which transits through the energy barrier by applying a moment M_i and returns with a moment M_f. To design the gripper, it is important to ensure the return moment (M_f) in the mechanism is high to facilitate a high load capacity of the gripper. This is achieved by introducing angular and translational stoppers, with their position selection described in details in SI-8. Angular stoppers define the limit of the rotation angle θ, while translational stoppers limit the displacement of strips to ensure they are at a position that generates the maximum return moment (M_f). Note that the transverse force F_y is much larger than F_x (see Fig. 2c) and consequently
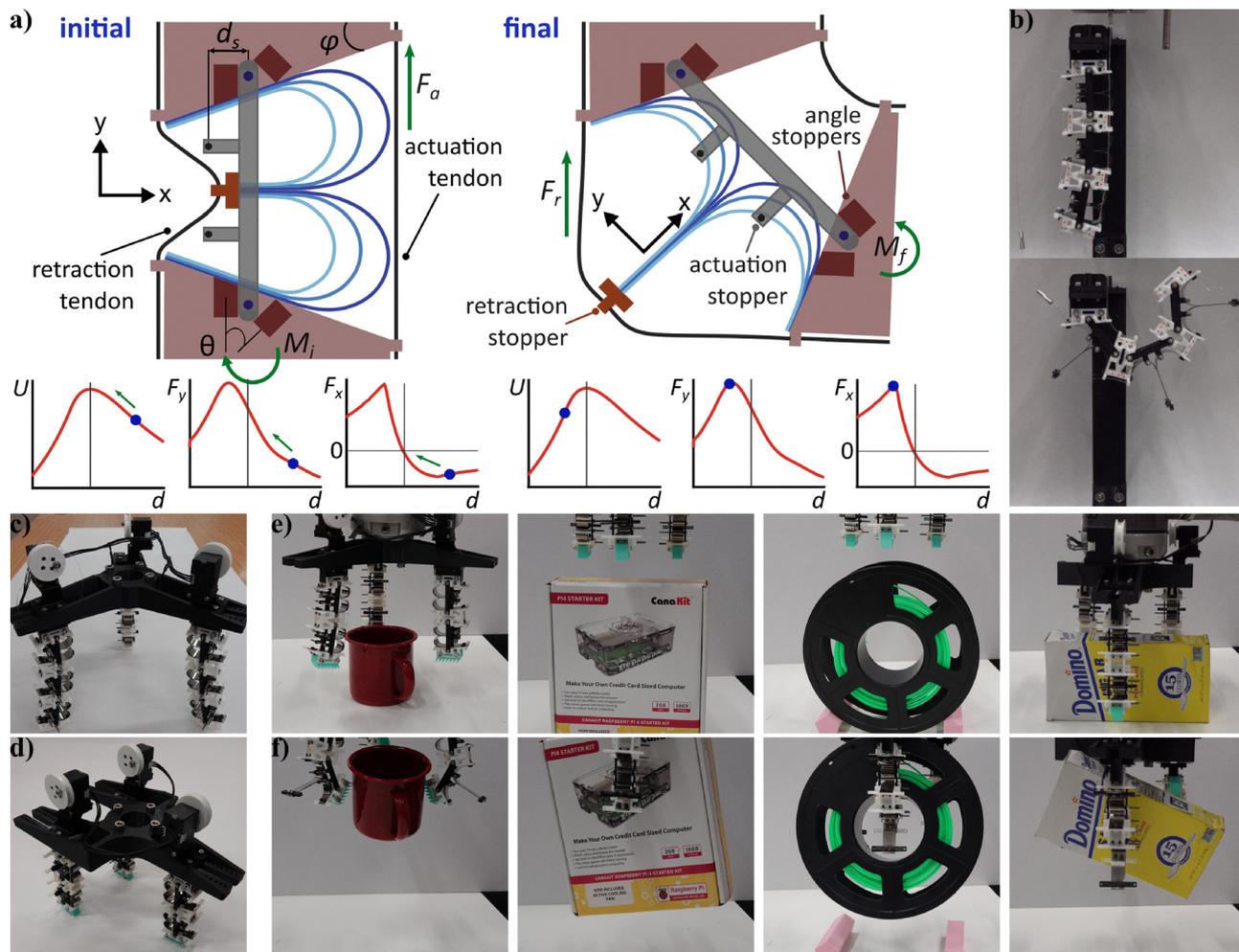
Fig. 6 Bistable gripper design. (a) Initial and final configurations of a gripper cell and nomenclature, plus strain energy and forces in each configuration (bottom). (b) Initial and final configuration of a three cell gripper finger with $\theta = 30°$ and $\varphi = 5°$. (c) Coaxial gripper configuration. (d) Tandem gripper configuration. (e) and (f) Gripping demonstration of four objects with different geometries, (e) before actuation and (f) after actuation.

return moment (M_f), hence the load capacity of the bistable mechanism in rotational motion could be potentially larger than in the case of linear motion applications.

Fig. 6b shows a gripper finger made of three cells in initial and final configurations where $\theta = 30°$ and $\varphi = 5°$, which results in a rotation angle of 70° per cell. Each cell weighs 54.4 g, and uses three pairs of stainless steel strips with $t = 100$ micron and $l = 73, 75, 77$ mm and 3D-printed wall segments. To evaluate the gripping performance of the bistable mechanism, two arrangements for installing fingers were considered: co-axial (Fig. 6c) and tandem (Fig. 6d) using two cells per finger. Gripping tests were undertaken on a range of objects using a robotic arm (see SI-8) including successfully grasping and lifting cylindrical mug, annular spool, and rectangular boxes (Fig. 6e and f).

2.5 Discussion

The rolling mechanism proposed here solves an important issue of bistable negative stiffness metamaterials by combining high force, high strain, and durability. These important features introduce some challenges for manufacturing and scalability.

Creating a tessellation of the proposed unit cell at the microscale, especially for multi-strip cases, is challenging. However, there are many applications such as dynamic systems and reusable energy absorption[85,86] and programming/encryption[33] at the larger scale, where the unit cell size can be on the order of millimeters. Using a combination of available manufacturing and assembly processes, functional homogeneous tessellations up to the decimeter/meter scale can be manufactured.

While manufacturing multi-strip units at the microscale is challenging, creating rolling prestressed single strip mechanisms has been demonstrated[61] using optical tweezers that enable micro-assembly. In addition, the rotational hinge at the microscale could be created using rotational compliant hinges[87] or compliant flexure hinge mechanisms.[88–90] Therefore, miniaturization of the proposed rolling metamaterials could be a topic of future studies. Considering these manufacturing and assembly challenges, scalable production and batch manufacturing is viable for mesoscale unit cells.

Like any other material or structure, environmental factors such as moisture, temperature, and corrosion affect the

performance of this metamaterial. If the metamaterial is made at the microscale, moisture might generate capillary forces that affect its force–displacement profile, disturb electrostatic actuation, and finally degrade the structure and performance by oxidation. However, at large scales such as mesoscale, the capillary forces are less of a concern. With higher or lower temperatures, the state of prestress in strips will affect the force–displacement profile, but bistability is governed by geometry and will be preserved. Corrosion is a concern for most metallic systems and the choice of material for the rotating walls and strips and the clamps between them should be studied to determine if any kind of corrosion, such as galvanic corrosion between strips and the walls, is a concern. On the manufacturing side, the bistability and rolling mechanism are generally robust, unless large misalignment between strips and walls disrupts rolling or causes stress concentration at the end constraints, resulting in plastic deformations or shortened life cycle.

In terms of constitutive material of the strips, a range of different materials can be used. It is important to note that the highest force density is achievable with materials with highest strength that allow large stress and curvature values in rolling strips, which is the reason for choosing the metallic strips in this study. For a constant maximum force or stress, the larger the strength of the material, the smaller the unit cell size or number of strips. To select other materials such as polymers or shape memory alloys (SMA) for rolling strips, the methodology developed in Supplementary Information SI-1.6 explains how the maximum stress in the strip for a certain angle θ and width W can be calculated. Knowing the maximum stress, the selection process would be: (i) choosing a material for a single strip that has a yield stress above the calculated maximum stress ($\sigma_y > \sigma_{\max}$), or (ii) choosing the material that has a fatigue limit stress above the calculated maximum stress ($\sigma_e > \sigma_{\max}$).

This metamaterial can be actuated beyond just electrostatic means, though its rolling-contact zipping points naturally lend themselves to electrostatic zipping. Other actuation methods could include the use of SMA or shape memory polymer (SMP) to rotate the walls and initiate snapping. SMA and SMP actuators can have very large specific power (up to 50 kW kg^{-1} due to high stress values), while their strain and work density are limited to 0.09 (10 000 kJ m^{-3}) and 0.49 (2850 kJ m^{-3}), respectively.[91–93] Pneumatic and DEA actuators also follow them by 2000 W kg^{-1} and 600 W kg^{-1} specific power, and strain/work density of 0.5 (500 kJ m^{-3}) and 0.79 (3500 KJ m^{-3}), respectively.[93–96] In liquid amplified electrostatic actuators, HASEL actuators reache peak power density of 614 W kg^{-1} with strains <0.42,[91,97] while DLZ provides a much larger strain capacity up to 0.99 and peak power of 103 W kg^{-1}.[68] Bandwidth is also an important factor in actuation performance, where snapping can increase the actuation speed and frequency. While SMA and SMP generate high power, they need time to cool down when used in cyclic actuation, hence, reducing bandwidth. Therefore, electrostatic and liquid amplified actuators are more suitable for faster actuation than SMA. Therefore, right actuation mechanism can be integrated into the bistable metamaterial to achieve the desired performance depending on the application. Displacement and force control for this type of actuator are difficult to operate. The system consists of binary actuators, which function resembling switches or logic gates, operating in two distinct states.

Future studies exploring this mechanism will cover different aspects such as dynamic response analysis and impact absorption, multi-parameter optimization, miniaturization and microscale manufacturing, large scale manufacturing, and other actuation methods and transduction mechanisms.

3 Conclusion

Here we present a novel rolling contact mechanical metamaterial as a solution for high force and high strain bistable device with long life cycle. Previously, long life cycle in bistable and negative stiffness metamaterials was achieved by sacrificing the force and/or strain, while with this proposed design, force and strain are not sacrificed. The principal working mechanism is bending and rolling of elastic strips inside a channel created by two rotating walls. While a unit cell is bistable with negative stiffness, a tessellation of the unit cells generates multistable metamaterial structures that provide hysteresis in a tension-compression cycle.

The long cyclic life and large strain are the result of the rolling mechanism. Rolling of strips can continue as long as their length permits within the range of walls, while the maximum stress in the strips depends on the channel width and angle. Therefore, peak stress that affects cyclic life can be limited without sacrificing strain. Using multiple strips, peak forces are multiplied by the number of strips without altering the unit cell volume, hence amplifying the force density and stiffness. Test results confirmed consistency of peak force values and bistability up to 10 000 cycles, while other bistable metamaterials lose their performance significantly at below 1000 cycles.[41,64]

The rolling mechanism architecture proposed in this work enables both linear motion through the strips and rotational motion through the walls, offering advantages in applications such as bio-inspired perching and rapid bistable grippers. In perching, the proposed mechanism achieves high resisting force of 56.9 N with much smaller activation force than previous literature using passive activation. This metamaterial not only provides a unique combination of mechanical properties in passive form, but also provides power and strain amplification as an active metamaterial. Electrostatic actuation was demonstrated as a suitable transduction mechanism, allowing the bistable metamaterial to function as a muscle-mimetic actuator.

The presented rolling mechanism opens a new avenues in the design space of mechanical metamaterials by allowing the combination of properties not previously achieved including high force, high strain, long cyclic life and amplified power. These properties are of great interest in many applications such as fast grippers in high speed robotic manufacturing and

assembly lines, active bistable devices in future biomedical implants, shape morphing and deployable structures.

4 Materials and methods

4.1 Mechanical tests

The metal strips were low-fatigue stainless steel (h + s präzisionsfolien gmbh, Germany) where yield stress of the $t = 100$, 150 micron samples was 2000–2200 MPa and $t = 200$ micron was 1800–2000 MPa, as reported by the manufacturer. The metal strips where punched at the two ends using a custom-made die and punch to create two holes for M3 bolts required for clamping strips together and to the walls. The tensile test setup was made by 3D-printing the walls and connecting components using a desktop FDM printer and PETG filament and laser cutting 5 mm thick acrylic sheet. Tensile tests were performed on an Instron 34SC-5 machine using a 100 N load cell. Tensile tests were performed for two tension/compression cycles with 100 mm min^{-1} speed where force–displacement diagrams of two cycles in both directions overlapped.

For the mechanical testing of the lattices, the maximum displacement of 330 mm was considered and test speed of 600 mm min^{-1} was used, with three cycles of tension/compression tests being performed. The displacement of the lattice along the out-of-plane direction was avoided by creating a prismatic channel on both sides as boundary condition, because under tension and compression the lattice is prone to buckling.

Cyclic life tests were performed at 600 mm min^{-1} for 10 000 cycles where each cycle had a 55 mm displacement. This means a period of 11 seconds for each tension-compression cycle and frequency of $f = 1/T = 1/11 \approx 0.09$ Hz. The test speed was constant and consistent over 10 000 cycles. The cyclic tests were performed using a set of strips with $t = 100$ micron, $l = 200$ mm, $L = 170$ mm, $W = 60$ mm and $\theta = 25°$. Four ball bearings were used as the hinges of the walls to ensure that the effect of contact at the hinges on the results are minimized. As the length was shorter than those used in tensile test characterization, the 100 micron strips did not buckle.

4.2 Actuation tests

The actuation tests were performed inside a high-voltage test rig. Actuation was controlled from a PC using a high-voltage amplifier (10HVA24-BP1, UltraVolt, USA), with the displacement measured by a laser displacement meter (LK-G402, Keyence, Japan) and all data was logged using a data acquisition unit (NI USB-6343, National Instruments, USA). The laser was installed above the setup and the beam was focused on the flat 3D-printed target connected to an acrylic clamp that constrained the strips at the bottom. The mass of the clamp and the target was 1.95 g, which was added to the mass loading when calculating isotonic actuation performance. The metal strips were connected to electrical ground and the conductive surface of the wall was connected to the 10 kV high voltage channel. The walls were laser-cut from 2 mm acrylic sheet and covered with conductive copper tape (RS, UK). Then two layers of PVC tape (AT7, Advance Tapes, UK) were applied to avoid short circuit where thickness of each layer is 130 micron. Silicone oil with 50 cst viscosity (Merck, Germany) was used as dielectric liquid.

4.3 Perching mechanism

Details of perching mechanism testing are presented in SI-7. The foot and claws were 3D-printed using desktop FDM printers using PLA. Targets with different diameters were also 3D-printed using PETG filament. The target were fixed to a stand which was connected to the base of the tensile test machine. To measure the moment capacity for different targets using tensile testing, a drum-shaped setup was designed that converted linear motion to rotary motion (see SI-7). The drone shown in the Fig. 5b has a gross mass of 2.15 kg including the perching feet.

4.4 Gripper details

The gripper segments were made of narrower stainless steel strips with $b = 12.7$ mm width. Fishing line (T400) with 0.45 mm diameter was used for tendons. The wall segments were 3D inkjet printed (Stratasys, USA) using Vero rigid material. The contact point at the end of fingers was a block of 3D-printed TPU (Shore A 85). Each finger of two segments was actuated using a Dynamixel XL330-M288-T servo motor controlled by an OpenRB-150 board. The bases of the gripper for co-axial and tandem configurations were 3D-printed using PETG filament and connected to the robot arm (UR10, Universal Robots) for gripping tests.

Conflicts of interest

There are no conflicts to declare.

Data availability

The data that support the findings of this study are available from the University of Bristol Data Repository at: [https://doi.org/10.5523/bris.m7u1djhkbq9e2qnm3dbbbwowt].

Supplementary information (SI): SI-1. Metamaterial design details. SI-2. Mechanical test details. SI-3. Finite element analysis details. SI-4. Lattice test details. SI-5. Multi strip design details. SI-6. Actuation study details. SI-7. Perching mechanism study details. SI-8. Gripper design details. SI-9. Codes. SV-1. Tensile test of the bistable mechanism. SV-2. Finite element analysis results. SV-3. Tensile test on lattice and multi-strip models. SV-4. Isotonic test of actuating unit cell. SV-5. Perching characterization. SV-6. Gripper tests. See DOI: https://doi.org/10.1039/d6mh00042h.

Acknowledgements

References

1 K. Bertoldi, V. Vitelli, J. Christensen and M. Van Hecke, *Nat. Rev. Mater.*, 2017, **2**, 1–11.

2 A. Rafsanjani, K. Bertoldi and A. R. Studart, *Sci. Robot.*, 2019, **4**, eaav7874.

3 D. Restrepo, N. D. Mankame and P. D. Zavattieri, *Extreme Mech. Lett.*, 2015, **4**, 52–60.

4 Y. Chen and L. Jin, *Adv. Funct. Mater.*, 2021, **31**, 2102113.

5 T. Frenzel, C. Findeisen, M. Kadic, P. Gumbsch and M. Wegener, *Adv. Mater.*, 2016, **28**, 5865–5870.

6 R. Khajehtourian and D. M. Kochmann, *Extreme Mech. Lett.*, 2020, **37**, 100700.

7 A. Rafsanjani, A. Akbarzadeh and D. Pasini, *arXiv*, 2016, preprint, arXiv:1612.05987, DOI: 10.48550/arXiv.1612.05987.

8 H. Mofatteh, B. Shahryari, A. Mirabolghasemi, A. Seyedkanani, R. Shirzadkhani, G. Desharnais and A. Akbarzadeh, *Adv. Sci.*, 2022, **9**, 2202883.

9 C. Qiao, F. Agnelli, D. K. Pokkalla, N. D'Ambrosio and D. Pasini, *Adv. Mater.*, 2024, 2313198.

10 M. E. Pontecorvo, S. Barbarino, G. J. Murray and F. S. Gandhi, *J. Intell. Mater. Syst. Struct.*, 2013, **24**, 274–286.

11 B. Shahryari, H. Mofatteh, A. Sargazi, A. Mirabolghasemi, D. Meger and A. Akbarzadeh, *Adv. Funct. Mater.*, 2024, 2407651.

12 S. Shan, S. H. Kang, J. R. Raney, P. Wang, L. Fang, F. Candido, J. A. Lewis and K. Bertoldi, *Adv. Mater.*, 2015, **27**, 4296–4301.

13 G. Wang, D. Li, W. Liao, T. Liu, X. Li, Q. An and Z. Qu, *Adv. Mater.*, 2024, 2408216.

14 Y. Chi, Y. Li, Y. Zhao, Y. Hong, Y. Tang and J. Yin, *Adv. Mater.*, 2022, **34**, 2110384.

15 Y. Cao, M. Derakhshani, Y. Fang, G. Huang and C. Cao, *Adv. Funct. Mater.*, 2021, **31**, 2106231.

16 Y. Forterre, J. M. Skotheim, J. Dumais and L. Mahadevan, *Nature*, 2005, **433**, 421–425.

17 E. Steinhardt, N.-s P. Hyun, J.-s Koh, G. Freeburn, M. H. Rosen, F. Z. Temel, S. Patek and R. J. Wood, *Proc. Natl. Acad. Sci. U. S. A.*, 2021, **118**, e2026833118.

18 J. T. Overvelde, T. Kloek, J. J. D'haen and K. Bertoldi, *Proc. Natl. Acad. Sci. U. S. A.*, 2015, **112**, 10863–10868.

19 Y. Chi, Y. Hong, Y. Zhao, Y. Li and J. Yin, *Sci. Adv.*, 2022, **8**, eadd3788.

20 Y. Liu, F. Pan, F. Xiong, Y. Wei, Y. Ruan, B. Ding, K. Yang and Y. Chen, *Adv. Funct. Mater.*, 2023, **33**, 2300433.

21 L. Jin, Y. Yang, B. O. T. Maldonado, S. D. Lee, N. Figueroa, R. J. Full and S. Yang, *Adv. Intell. Syst.*, 2023, **5**, 2300039.

22 T. Bambrick, A. Viquerat and R. Siddall, *Adv. Intell. Syst.*, 2024, 2300748.

23 H. Shao, S. Wei, X. Jiang, D. P. Holmes and T. K. Ghosh, *Adv. Funct. Mater.*, 2018, **28**, 1802999.

24 B. Li, L. Jiang, W. Ma, Y. Zhang, W. Sun and G. Chen, *Adv. Intell. Syst.*, 2022, **4**, 2100188.

25 B. D. Jensen, L. L. Howell and L. G. Salmon, International Design Engineering Technical Conferences and Computers and Information in Engineering Conference, 1998, p. V01AT01A003.

26 M. T. A. Saif, *J. Microelectromech. Syst.*, 2000, **9**, 157–170.

27 H. Matoba, T. Ishikawa, C.-J. Kim and R. S. Muller, Proceedings IEEE Micro Electro Mechanical Systems An Investigation of Micro Structures, Sensors, Actuators, Machines and Robotic Systems, 1994, pp. 45-50.

28 E. Kruglick and K. S. Pister, *Solid-State Sensor and Actuator Workshop*, 1998.

29 Y. Gerson, S. Krylov and B. Ilic, *J. Micromech. Microeng.*, 2010, **20**, 112001.

30 J. Casals-Terre, A. Fargas-Marques and A. M. Shkel, *J. Microelectromech. Syst.*, 2008, **17**, 1082–1093.

31 P. Rothemund, A. Ainla, L. Belding, D. J. Preston, S. Kurihara, Z. Suo and G. M. Whitesides, *Sci. Robot.*, 2018, **3**, eaar7986.

32 C. Qiao, L. Liu and D. Pasini, *Adv. Sci.*, 2021, **8**, 2100445.

33 T. Chen, M. Pauly and P. M. Reis, *Nature*, 2021, **589**, 386–390.

34 Z. Chen, S. Kong, Y. He, S. Chen, W. Wang, L. Jin, S. Zhang, Y. Hong, L. Pan and H. Wu, *et al.*, *Adv. Funct. Mater.*, 2024, **34**, 2311498.

35 E. Kebadze, S. Guest and S. Pellegrino, *Int. J. Solids Struct.*, 2004, **41**, 2801–2820.

36 B. Gorissen, D. Melancon, N. Vasios, M. Torbati and K. Bertoldi, *Sci. Robot.*, 2020, **5**, eabb1967.

37 D. Tang, C. Zhang, C. Pan, H. Hu, H. Sun, H. Dai, J. Fu, C. Majidi and P. Zhao, *Sci. Robot.*, 2024, **9**, eadm8484.

38 R. Ma, L. Wu and D. Pasini, *Adv. Funct. Mater.*, 2023, **33**, 2213371.

39 H. Yang, N. D'Ambrosio, P. Liu, D. Pasini and L. Ma, *Mater. Today*, 2023, **66**, 36–49.

40 W. Li, F. Wang, O. Sigmund and X. S. Zhang, *Proc. Natl. Acad. Sci. U. S. A.*, 2022, **119**, e2120563119.

41 X. Shang, L. Liu, A. Rafsanjani and D. Pasini, *J. Mater. Res.*, 2018, **33**, 300–308.

42 S. Wu, Q. Ze, J. Dai, N. Udipi, G. H. Paulino and R. Zhao, *Proc. Natl. Acad. Sci. U. S. A.*, 2021, **118**, e2110023118.

43 D. Melancon, B. Gorissen, C. J. Garca-Mora, C. Hoberman and K. Bertoldi, *Nature*, 2021, **592**, 545–550.

44 D. Melancon, A. E. Forte, L. M. Kamp, B. Gorissen and K. Bertoldi, *Adv. Funct. Mater.*, 2022, **32**, 2201891.

45 T. Chen, O. R. Bilal, K. Shea and C. Daraio, *Proc. Natl. Acad. Sci. U. S. A.*, 2018, **115**, 5698–5702.

46 Y. Tang, Y. Chi, J. Sun, T.-H. Huang, O. H. Maghsoudi, A. Spence, J. Zhao, H. Su and J. Yin, *Sci. Adv.*, 2020, **6**, eaaz6912.

47 S. Ahmadi, R. Hedayati, Y. Li, K. Lietaert, N. Tümer, A. Fatemi, C. Rans, B. Pouran, H. Weinans and A. Zadpoor, *Acta Biomater.*, 2018, **65**, 292–304.

48 S. Ahmadi, R. Kumar, E. Borisov, R. Petrov, S. Leeflang, Y. Li, N. Tümer, R. Huizenga, C. Ayas and A. Zadpoor, *et al.*, *Acta Biomater.*, 2019, **83**, 153–166.

49 H. Huang, L. Wang and Y. Fan, *J. Sci.:Adv. Mater. Devices*, 2023, **8**, 100585.

50 H. Kolken, A. F. Garcia, A. Du Plessis, A. Meynen, C. Rans, L. Scheys, M. J. Mirzaali and A. Zadpoor, *Acta Biomater.*, 2022, **138**, 398–409.

51 H. Kolken, A. F. Garcia, A. Du Plessis, C. Rans, M. J. Mirzaali and A. Zadpoor, *Acta Biomater.*, 2021, **126**, 511–523.

52 N. D. Masters and L. L. Howell, *J. Microelectromech. Syst.*, 2003, **12**, 273–280.

53 X. Chen, D. Du, B. Wang, S. Jiang, C. Guan and S. Zhong, *Mater. Lett.*, 2024, **368**, 136697.

54 S. A. Chowdhury, S. Li and O. J. Myers, *J. Compos. Mater.*, 2023, **57**, 4275–4289.

55 L. Howell, S. Rao and A. Midha, International Design Engineering Technical Conferences and Computers and Information in Engineering Conference, 1993, pp. 441-448.

56 A. S. Meeussen, G. Bordiga, A. X. Chang, B. Spoettling, K. P. Becker, L. Mahadevan and K. Bertoldi, *Adv. Funct. Mater.*, 2024, 2415986.

57 D. F. Wilkes, *Rolamite: A New Mechanical Design Concept*, Sandia national lab.(snl-nm), albuquerque, nm (united states) technical report, 1969.

58 B. M. Hillberry and A. S. Hall Jr, *Rolling contact prosthetic knee joint*, 1976, US Pat., 3,945,053.

59 P. A. Halverson, L. L. Howell and S. P. Magleby, *Mech. Mach. Theory*, 2010, **45**, 147–156.

60 J. Cai and J. Feng, *Smart Mater. Struct.*, 2014, **23**, 045011.

61 L. A. Shaw, S. Chizari, M. Dotson, Y. Song and J. B. Hopkins, *Nat. Commun.*, 2018, **9**, 4594.

62 S. Janbaz, F. Bobbert, M. J. Mirzaali and A. A. Zadpoor, *Mater. Horiz.*, 2019, **6**, 1138–1147.

63 J. Qi, Z. Chen, P. Jiang, W. Hu, Y. Wang, Z. Zhao, X. Cao, S. Zhang, R. Tao and Y. Li, *et al.*, *Adv. Sci.*, 2022, **9**, 2102662.

64 H.-D. Kim, Y.-J. Kang and Y. Noh, *Smart Mater. Struct.*, 2025, **34**, 075038.

65 F. Rothfischer, L. J. Weiß, N. Tedeschi, M. Matthies, M. Vogt, C. Karfusehr, A. Hebel, P. Šulc, T. Liedl, E. Kopperger, *et al.*, *arXiv*, 2025, preprint, arXiv:2505.10544, DOI: 10.48550/arXiv.2505.10544.

66 M. Caruel, J.-M. Allain and L. Truskinovsky, *Phys. Rev. Lett.*, 2013, **110**, 248103.

67 A. F. Huxley and R. M. Simmons, *Nature*, 1971, **233**, 533–538.

68 M. Taghavi, T. Helps and J. Rossiter, *Sci. Robot.*, 2018, **3**, eaau9795.

69 P. Rothemund, N. Kellaris, S. K. Mitchell, E. Acome and C. Keplinger, *Adv. Mater.*, 2021, **33**, 2003375.

70 M. Ilton, M. S. Bhamla, X. Ma, S. M. Cox, L. L. Fitchett, Y. Kim, J.-S. Koh, D. Krishnamurthy, C.-Y. Kuo and F. Z. Temel, *et al.*, *Science*, 2018, **360**, eaao1082.

71 M. Taghavi, T. Helps and J. Rossiter, 2020 IEEE International Conference on Robotics and Automation (ICRA), 2020, pp. 5856-5861.

72 S. Bluett, T. Helps, M. Taghavi and J. Rossiter, *IEEE Robot. Autom. Lett.*, 2020, **5**, 3931–3936.

73 Z. Yoder, D. Macari, G. Kleinwaks, I. Schmidt, E. Acome and C. Keplinger, *Adv. Funct. Mater.*, 2023, **33**, 2209080.

74 C. Kaspar, B. J. Ravoo, W. G. van der Wiel, S. V. Wegner and W. H. Pernice, *Nature*, 2021, **594**, 345–355.

75 M. Garrad, M. N. Zadeh, C. Romero, F. Scarpa, A. T. Conn and J. Rossiter, *IEEE Robot. Autom. Lett.*, 2022, **7**, 3938–3944.

76 M. N. Zadeh, M. Garrad, C. Romero, A. Conn, F. Scarpa and J. Rossiter, *IEEE Robot. Autom. Lett.*, 2022, **7**, 10352–10358.

77 K. Hang, X. Lyu, H. Song, J. A. Stork, A. M. Dollar, D. Kragic and F. Zhang, *Sci. Robot.*, 2019, **4**, eaau6637.

78 W. R. Roderick, M. R. Cutkosky and D. Lentink, *Sci. Robot.*, 2021, **6**, eabj7562.

79 H. Zhang, J. Sun and J. Zhao, 2019 International Conference on Robotics and Automation (ICRA), 2019, pp. 1248-1253.

80 H. Hsiao, J. Sun, H. Zhang and J. Zhao, *IEEE/ASME Trans. Mech.*, 2022, **27**, 5243–5253.

81 R. Zufferey, J. Tormo-Barbero, D. Feliu-Talegón, S. R. Nekoo, J. Á. Acosta and A. Ollero, *Nat. Commun.*, 2022, **13**, 7713.

82 W. Stewart, L. Guarino, Y. Piskarev and D. Floreano, *Adv. Intell. Syst.*, 2023, **5**, 2100150.

83 P. H. Nguyen, K. Patnaik, S. Mishra, P. Polygerinos and W. Zhang, *Soft Robot.*, 2023, **10**, 838–851.

84 L. Zhou, L. Ren, Y. Chen, S. Niu, Z. Han and L. Ren, *Adv. Sci.*, 2021, **8**, 2002017.

85 A. Shaw, S. Neild, D. Wagg, P. Weaver and A. Carrella, *J. Sound Vib.*, 2013, **332**, 6265–6275.

86 H. Yang, J. Zhang, J. Wang, J. Hu, Z. Wu, F. Pan and J. Wu, *Adv. Funct. Mater.*, 2025, **35**, 2410217.

87 R. M. Fowler, *Investigation of compliant space mechanisms with application to the design of a large-displacement monolithic compliant rotational hinge*, Brigham Young University, 2012.

88 F. Dirksen and R. Lammering, *Mech. Sci.*, 2011, **2**, 109–117.

89 Y. Tian, B. Shirinzadeh, D. Zhang and Y. Zhong, *Precis. Eng.*, 2010, **34**, 92–100.

90 G. Chen and L. L. Howell, *Precis. Eng.*, 2009, **33**, 268–274.

91 E. Acome, S. K. Mitchell, T. Morrissey, M. Emmett, C. Benjamin, M. King, M. Radakovitz and C. Keplinger, *Science*, 2018, **359**, 61–65.

92 C. S. Haines, M. D. Lima, N. Li, G. M. Spinks, J. Foroughi, J. D. Madden, S. H. Kim, S. Fang, M. Jung de Andrade and F. Göktepe, *et al.*, *Science*, 2014, **343**, 868–872.

93 S. M. Mirvakili and I. W. Hunter, *Adv. Mater.*, 2018, **30**, 1704407.

94 D. R. Higueras-Ruiz, K. Nishikawa, H. Feigenbaum and M. Shafer, *Bioinspiration Biomimetics*, 2021, **17**, 011001.

95 S. Li, D. M. Vogt, D. Rus and R. J. Wood, *Proc. Natl. Acad. Sci. U. S. A.*, 2017, **114**, 13132–13137.

96 D. R. Higueras-Ruiz, M. W. Shafer and H. P. Feigenbaum, *Sci. Robot.*, 2021, **6**, eabd5383.

97 X. Wang, S. K. Mitchell, E. H. Rumley, P. Rothemund and C. Keplinger, *Adv. Funct. Mater.*, 2020, **30**, 1908821.